Tunable Synaptic Plasticity in Europium 2-D Perovskite ReRAM With Sub-0.5 V Switchings

Manvendra Chauhan and Satinder K. Sharma, *Senior Member, IEEE*

***Abstract*— Lead-free, and reliable resistive switching (RS) materials are essential for next-generation resistive random access memory (ReRAM) and neuromorphic computing, where low programming voltage, environmental compliance, and multifunctional stability are essential. Two-dimensional (2-D) perovskites portend a promising materials class owing to moisture resistance, scalable solution processability, and the ability to modulate interface energy-level alignment, positioning them as attractive candidates for multifunctional switching layers (SLs). In this work, europium (Eu)-based 2-D perovskite thin films were systematically tailored through precursor stoichiometry control to correlate microstructural, crystallographic, and surface electronic properties with RS behavior. Progressive transition from porous, defect-rich surfaces to compact, pinhole-free films with enhanced ordering was observed. Ag-electrode-based devices fabricated on the optimized films exhibited forming-free, symmetric bipolar RS with sub-volt thresholds, considerably large memory windows, retention beyond 10^4 s, and endurance exceeding 4×10^4 cycles. Comparative studies with inert and easily oxidized electrodes confirmed an electrochemical metallization (ECM) process, governed by Ag^+ migration and reduction, as the dominant RS mechanism. Neuromorphic evaluation under varied programming pulses revealed a dynamic trade-off; longer pulses expanded dynamic range (DR) but induced higher potentiation nonlinearity, while shorter pulses suppressed filament overgrowth, yielding near-linear weight updates with low nonlinearity index (NLI). Such tunability enables task-specific optimization of synaptic plasticity, where large DR supports classification accuracy and high linearity benefits analog computing. These findings establish Eu-based 2-D perovskites as a lead-free, reliable platform for low-power ReRAM and high-fidelity neuromorphic systems.**

***Index Terms*— Artificial synapse, lead-free, nonlinearity index, resistive memory, two-dimensional (2-D) perovskite.**

I. Introduction

With the progression of big data technologies and the rise of deep learning leveraging advanced neural networks, there is an escalating demand for enhanced computational throughput beyond traditional central processing units (CPUs), especially phenomena pertaining to human–computer interaction (HCI), artificial intelligence (AI), and intelligent augmentation (IA).

As semiconductor devices continue to shrink toward their physical scaling limits, manufacturing becomes increasingly expensive and technologically demanding, slowing the long-established progression associated with Moore's law. In this context, resistive RAM (ReRAM) has gained considerable attention as a next-generation non-volatile (NV) memory. Its ability to mimic synaptic behavior and support vertically stacked, 3-D architectures makes it a promising candidate for energy-efficient neuromorphic systems capable of easing both the constraints of Moore-scale integration and the von Neumann communication bottleneck [1], [2]. These trends underscore the growing need to rethink conventional computing architectures.

In recent years, neuromorphic computing has become a leading direction for next-generation information processing, as it seeks to emulate the interconnected structure and signal-processing capabilities of biological neural networks directly in hardware. Such systems can perform tasks like real-time learning, pattern classification, and decision-making with remarkable speed and minimal energy use [3]. Hence, it can process a large amount of information in parallel, with extremely low-power consumption.

Lately, 3-D perovskites have attracted considerable interest due to their favorable charge-transport and optical properties, making them suitable for ReRAM technologies [4]. Despite these advantages, 3-D systems suffer from several drawbacks, such as the mobility of the methylammonium (MA^+) cation, difficulty in achieving stable multilevel switching, and vulnerability to moisture [5]. These limitations have motivated the exploration of two-dimensional (2-D) perovskites, where alternating organic and inorganic layers provide anisotropic transport pathways, significantly better moisture tolerance, greater photo-thermal robustness, and reduced ionic drift [6], [7]. Introducing bulky organic cations like phenethylammonium (PEA^+) further suppresses MA^+-related instability and enhances both environmental and thermal endurance in ReRAM devices [8]. Nevertheless, the substantial Pb content in these materials raises environmental and health concerns, prompting a strong shift toward investigating lead-free 2-D perovskite systems for next-generation ReRAM applications [9].

Though achieving high-quality, uniform lead-free perovskite films has been challenging. Issues with the large area film formation, crystallinity ordering, and defect control can result in nonreproducible electrical switching. Variations in

Received 5 September 2025; revised 13 November 2025; accepted 24 November 2025. Date of publication 11 December 2025; date of current version 6 January 2026. The review of this article was arranged by Editor D. Ielmini. *(Corresponding author: Satinder K. Sharma.)*

The authors are with the School of Computing and Electrical Engineering (SCEE), IIT Mandi, Mandi, Himachal Pradesh 175075, India (e-mail: satinder@iitmandi.ac.in).

This article has supplementary downloadable material available at https://doi.org/10.1109/TED.2025.3639201, provided by the authors.

Digital Object Identifier 10.1109/TED.2025.3639201

ionic radii, as well as in material synthesis and processing techniques, contribute to these inconsistencies. The metal cation, Europium (Eu) ions Eu^{3+}, has been considered as a promising lead-free alternative due to its ionic radius (~1.26Å in 8-coordination) [10] close to Pb^{2+} (~1.29Å for an 8-coordinate environment) [11], as well as its higher stability under ambient conditions compared to other Pb-free alternatives [such as tin (Sn) and bismuth (Bi)] that are widely utilized in perovskites [9]. Thus, substituting Pb ions with Eu ions in 2-D perovskites offers a more viable alternative compared to Sn- and Bi. Although lanthanide (Ln) based perovskites have recently demonstrated outstanding photonic and significant potential in optoelectronic applications [12]. The utilization of Ln ions in 2-D perovskite-based optoelectronic ReRAM remains unexplored. This knowledge gap presents a valuable opportunity to investigate the use of Ln ions in the performance and stability enhancement of Pb-free 2-D perovskite ReRAM systems.

Hence, in this work, we address this gap by systematically engineering Eu-based 2-D perovskite thin films through controlled precursor stoichiometry of PEABr:$EuBr_3$ molarity ratio to simultaneously optimize microstructure, crystallinity ordering, and interfacial energetics for high-performance resistive switching (RS) and neuromorphic operation. Detailed morphological, structural, optical, and surface potential analyses are correlated with device-level metrics to elucidate the role of stoichiometry in RS threshold and stability. Electrical characterization of the optimized Ag/PEABr:$EuBr_3$/FTO, ReRAM device structures reveal forming-free, symmetric bipolar switching at <0.5 V operation, with enhanced retention, endurance, and a considerably large memory window for the optimized composition. The electrode-dependent measurements further verify an ECM-driven mechanism, where Ag^+ transport and subsequent reduction govern the SET and RESET transitions. In addition, we examine how variations in pulsewidth influence the dynamic range (DR) and potentiation linearity (NLI%), showing that the timing of the programming pulses can be used to deliberately tune synaptic behavior. Overall, this work introduces a truly lead-free switching layer (SL) and provides practical guidelines that connect composition control, interfacial energetics, and pulse-engineering strategies to the resulting multifunctional ReRAM characteristics.

A. Preparation of 2-D Perovskite Formulations

Four sets of precursor solution samples were synthesized with varying molar ratios of phenethylammonium bromide (PEABr) to Europium (III) bromide ($EuBr_3$). In the first sample, the molar ratio was 1:1, with 0.5 mM amounts for each of PEABr and $EuBr_3$. In the second sample, the molar ratio was increased to 2:1. Similarly, for the third and fourth sets of perovskite formulations, the molar ratio was kept as 3:1 and 4:1, respectively. Each precursor mixture was dissolved separately in a 9:1 dimethylformamide (DMF) and dimethyl sulfoxide (DMSO) solvent solution at 70 °C and 300 r/min constant stirring for 4 h.

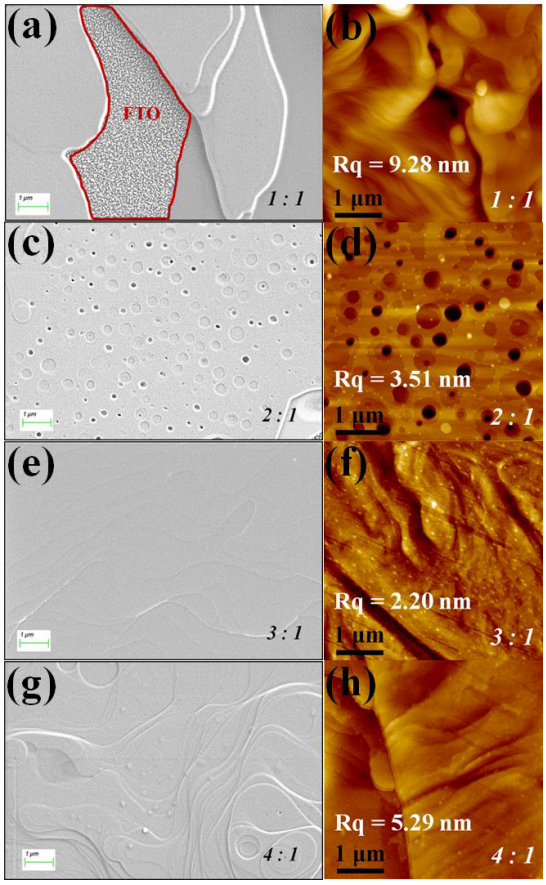

Fig. 1. FESEM and AFM micrographs of Eu-based 2-D perovskite films prepared with different PEABr:$EuBr_3$ precursor ratios: (a) and (b) 1:1, (c) and (d) 2:1, (e) and (f) 3:1, and (g) and (h) 4:1. Scale bar: 1 μm.

B. Thin Film Deposition and Device Fabrication

The ReRAM devices were fabricated on commercial FTO-coated glass substrates. These substrates were sequentially sonicated in deionized water, 2-propanone, and propane-2-ol for 15 min each, followed by 30 min surface treatment under UV/Ozone prior to thin-film deposition. Precursor solutions with the specified molarities were spin-coated onto the FTO substrates at 6000 r/min for 50 s, using toluene as an antisolvent. The deposited 2-D perovskite thin films were then treated at 90 °C for 30 min and finally annealed at 100 °C for 5 min. All the deposition and processing steps were performed inside an inert glovebox, maintaining a nitrogen atmosphere.

Afterward, Ag was deposited over the coated FTO wafers through shadow masking using the thermal evaporator. The deposited Ag acts as the top electrodes (TEs); meanwhile, FTO acts as the back electrode (BE) in the fabricated device configuration incorporating Eu-based 2-D perovskite SL.

II. Results and Discussion

The surface morphology of Eu-based 2-D perovskite thin films was found to be strongly dependent on the precursor stoichiometry, as revealed by field-emission scanning electron microscopy (FESEM) and atomic force microscopy (AFM) analyses (Fig. 1). For the 1:1 PEABr:$EuBr_3$ ratio, the FESEM image [Fig. 1(a)] shows poor surface coverage with large voids and exposed FTO regions, indicating incomplete nucleation

and insufficient film growth during spin-coating, arising from a suboptimal organic-to-inorganic ratio, where the limited supply of bulky PEA^+ cations fails to adequately suppress uncontrolled grain growth, leading to inhomogeneous crystallization, localized Eu-rich agglomeration, and the formation of electrically vulnerable voids that act as leakage pathways. The corresponding AFM topography [Fig. 1(b)] exhibits a high root-mean-square root mean squares (rms) roughness (Rq) of 9.28 nm, corroborating the observed nonuniform coverage. Increasing the organic content to a 2:1 $PEABr:EuBr_3$ ratio resulted in visibly compact film coverage, with fewer voids and narrower surface crevices [Fig. 1(c)]. This improvement is consistent with better grain-boundary passivation provided by the additional PEA^+ species, which is also reflected in the AFM-measured roughness [$Rq \sim$ 3.51 nm, Fig. 1(d)]. At the 3:1 composition, the FESEM image [Fig. 1(e)] reveals a continuous and highly uniform surface with no observable pinholes. Such a morphology indicates that an adequate amount of PEA^+ stabilizes Eu–Br octahedral growth, limits defect clustering, and promotes homogeneous grain packing. This is in agreement with the lowest roughness among all samples [$Rq \sim$ 2.20 nm, Fig. 1(f)]. When the PEA^+ content was further increased to 4:1, the film quality deteriorated. The FESEM micrograph [Fig. 1(g)] shows isolated, island-like regions and fluctuations in film thickness. These irregularities are likely caused by excess PEA^+ segregating out of the perovskite framework, creating organic-rich pockets that disturb the crystallization process [13]. The corresponding AFM image [Fig. 1(h)] confirms a higher surface roughness ($Rq \sim$ 5.29 nm). Taken together, the films evolve from incomplete and porous at 1:1 to denser and more uniform at 2:1 and 3:1, followed by a loss of uniformity at 4:1. This behavior reflects the dual role of PEA^+ in modulating nucleation and growth: moderate excess supports defect passivation and orderly crystal formation, while too much organic content disrupts lattice development and leads to phase separation and increased roughness.

The schematic in Fig. 2(a) depicts the anticipated arrangement of the $PEABr:EuBr_3$ layered perovskite. In this structure, inorganic $EuBr_6$ octahedra form stacked slabs that are periodically spaced by organic PEA^+ cations. Because each PEA^+ molecule contains a single ammonium group, it effectively terminates growth along the c-axis and inserts an organic layer between adjacent $EuBr_6$ sheets. This layered stacking produces the strong low-angle diffraction features seen in the X-ray diffraction (XRD) patterns.

The crystallographic characteristics of $PEABr:EuBr_3$ thin films with varying organic-to-inorganic molar ratios (1:1, 2:1, 3:1, and 4:1) were examined using XRD, as shown in Fig. 2(b). All compositions exhibit a prominent low-angle diffraction peak at $2\theta - 5.20°$, corresponding to the first-order out-of-plane reflection of the 2-D Ruddlesden–Popper (RP) perovskite phase [14], [15] (commonly indexed as (001) or (002) depending on the chosen unit cell setting) [15]. This reflection arises from the periodic stacking of organic–inorganic bilayers, confirming the formation of an ordered layered structure. While the (001) peak persists across all compositions, its intensity and sharpness improve progressively with higher

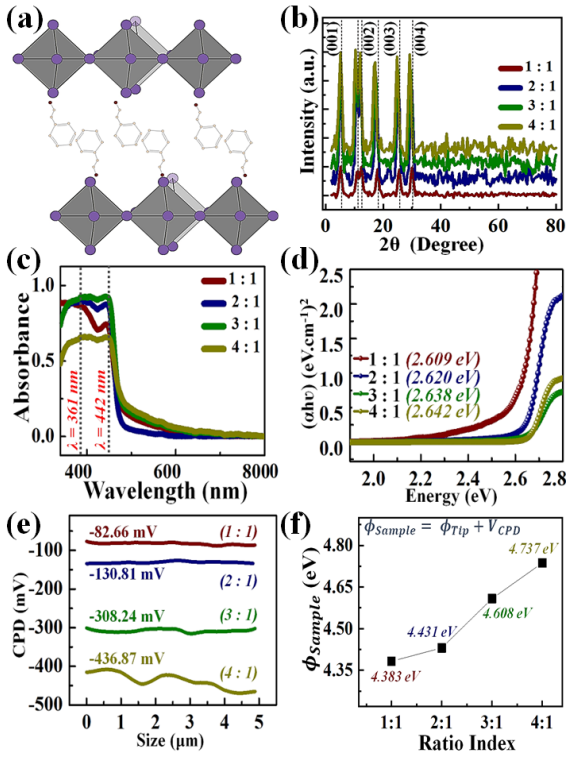

Fig. 2. (a) Schematic of the RP–type 2-D perovskite $PEABr:EuBr_3$, showing alternating $EuBr_6$ octahedral layers and organic PEA^+ spacer layers. The single-ammonium-group PEA^+ cation separates the inorganic slabs along the c-axis, forming a periodic layered structure. Effect of $PEABr:EuBr_3$ precursor ratio on (b) XRD patterns, (c) UV Absorbance spectra, (d) optical bandgap evolution, (e) CPD distribution, and (f) corresponding work function values, highlighting the correlation between composition, structure, and surface electronic properties.

PEABr content. In the 1:1 and 2:1 film, additional reflections appear at ~11.00° and ~12.40°, corresponding to the (100) and (001) planes of residual hexagonal $EuBr_3$ with a $PuBr_3$-type structure (a = 8.02Å, c = 7.14Å) [16].

These peaks indicate incomplete incorporation of Eu^{3+} into the perovskite lattice at lower organic content. With increasing PEABr concentration, 3:1 to 4:1, these $EuBr_3$-related peaks reduced markedly, suggesting improved coordination of PEA^+ with $[EuBr_6]^{3-}$ octahedra and enhanced phase purity. Moreover, the $EuBr_3$-related peaks show systematic low-angle shifts (from 11.00° to ~10.40° for (100), and from 12.40° to ~11.90° for (001) as the ratio increases from 1:1 to 4:1), indicating an expansion in interplanar spacing [17]. This can be attributed to lattice strain induced by partial PEA^+ intercalation and altered octahedral tilting in the layered matrix. At higher diffraction angles (18°–30°), weak higher-order (002)–(004) reflections are more pronounced in the 3:1 and 4:1 film, further confirming layered periodicity. However, the 4:1 film exhibits slight peak broadening and elevated background intensity, implying the onset of orientational disorder or partial amorphization due to excess PEA^+.

The UV–Vis's absorption spectra of $PEABr:EuBr_3$ thin films with different organic-to-inorganic ratios (1:1, 2:1, 3:1, and 4:1) are shown in Fig. 2(c). All films exhibit a distinct absorption onset in the UV region between $\lambda \approx$ 361 and 442 nm, corresponding to direct electronic transitions within the Eu–Br octahedral network.

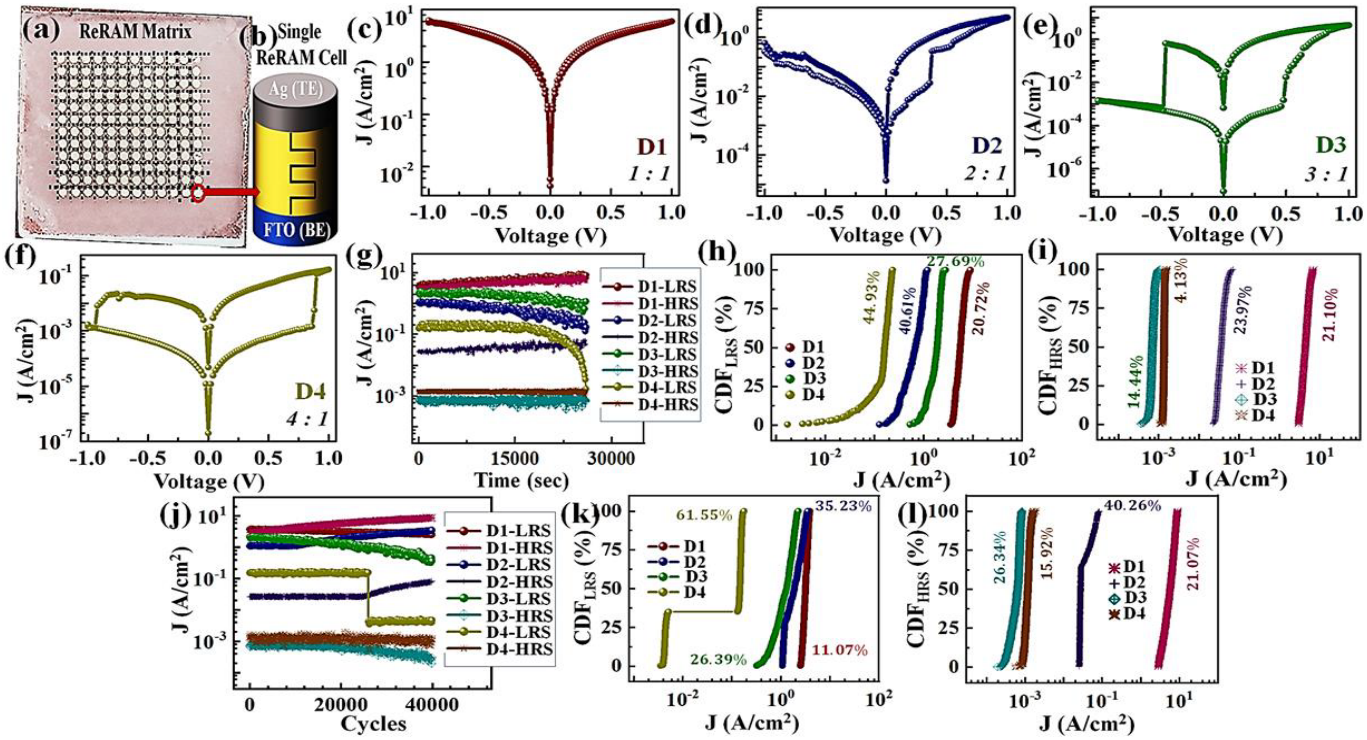

Fig. 3. (a) Optical micrographs of the fabricated ReRAM matrix, and (b) schematic illustration of single ReRAM cell configuration. dc RS characteristics of devices with varying stoichiometry: (c) *J–V* curve of D1 (1:1) showing no RS due to poor film quality and leakage. (d) *J–V* curve of D2 (2:1) showing low-voltage SET, incomplete RESET, and leakage in HRS. (e) *J–V* curve of D3 (3:1) showing stable, symmetric bipolar RS with high LRS/HRS ratio. (f) *J–V* curve of D4 (4:1) showing bipolar RS with higher switching voltages and reduced memory window. (g) Retention of D1–D4 at V_{READ} = 0.1 V for 26 000 s, with D3 showing best stability. (h) and (i) Statistical variability (σ/μ %) of LRS and HRS over retention, lowest for D3. (j) Endurance of D1–D4 over 40 000 cycles, with D3 maintaining a large memory window. (k) and (l) Statistical variability (σ/μ%) of LRS and HRS over endurance, lowest for D3.

Optical band gaps (E_g) were extracted from Tauc plots [Fig. 2(d)] using the relation

$$\alpha h\nu = A\left(h\nu - E_g\right)^n \tag{1}$$

where α, h, and ν are the absorption coefficient, Planck's constant, and incident photon frequency, respectively. The optical bandgap is denoted by E_g, and A is the proportionality constant. The estimated E_g, values are 2.609 eV (1:1), 2.620 eV (2:1), 2.638 eV (3:1), and 2.642 eV (4:1). This blueshift in the optical bandgap with increasing PEABr content is consistent with enhanced quantum confinement in layered RP perovskites; E_g decreases with increasing n (i.e., slab thickness) [15], [18], which suggests that the effective inorganic layer becomes thinner as bulkier PEA^+ cations terminate perovskite growth and reduce slab continuity.

Kelvin probe force microscopy (KPFM) measurements were performed to evaluate the surface potential (Ψ) and corresponding contact potential difference (CPD) for each composition. The measured CPD values were −82.66 mV (1:1), −130.81 mV (2:1), −308.24 mV (3:1), and −436.87 mV (4:1), as shown in Fig. 2(e). In KPFM, CPD reflects the difference in work function between the conductive AFM tip and the sample surface, following the relation

$$\phi_{\text{Sample}} = \phi_{\text{Tip}} + V_{\text{CPD}} \tag{2}$$

where ϕ_{Sample} and ϕ_{Tip} are the work functions of the deposited thin film samples and the tip (ϕ_{Tip} = 4.3 eV) used for KPFM measurements, respectively. The calculated ϕ_{Sample} values are 4.383 eV (1:1), 4.431 eV (2:1), 4.608 eV (3:1), and 4.737 eV (4:1) [Fig. 2(f)]. The progressive increase in ϕ_{Sample} with higher PEABr content corresponds to a systematic upward shift of the vacuum energy level relative to the Fermi level. This shift is attributed to the formation and alignment of interfacial dipoles by PEA^+ cations. PEA^+, with a positively charged ammonium head and neutral hydrophobic tail, preferentially aligns at the perovskite surface so its dipole points from the $[EuBr_6]^{3-}$ layers toward vacuum, creating an interfacial potential step that raises (E_{Vac}) and increases ϕ_{Sample} [19]. As the PEABr:$EuBr_3$ ratio increases, the surface coverage of PEA^+ becomes more complete, strengthening the net dipole field and producing larger negative CPD values.

The resulting upward shift of (E_{Vac}) relative to the Fermi level modifies the Schottky barrier height/energy barrier for charge injection at the metal-perovskite interface [20]. Such interfacial modulation is expected to influence the initiation and rupture of conductive pathways, thereby affecting set/reset thresholds, switching stability, and data retention. Thus, tuning the surface work function via PEABr concentration offers a means to tailor interfacial energetics, carrier injection efficiency, and overall RS switching characteristics of PEABr:$EuBr_3$-based ReRAM devices.

Anchored with these materials insights, the RS behavior of Ag/PEABr:$EuBr_3$/FTO devices was evaluated using a Keithley 4200-SCS semiconductor parameter analyzer. The prototype crossbar array matrix for ReRAM structures' micrograph captured through the cellular camera is presented in Fig. 3(a),

where FTO is the common BE and the TE Ag for all the ReRAM matrix representing each device as a single ReRAM cell with device area 0.0025 cm^2 as illustrated in Fig. 3(b). The black dashed line in Fig. 3(a) represents the physical separations between the individual ReRAM cells within the matrix. The architecture, although simple, is yet critical way for illustrating the organization of the array matrix, which facilitates the functioning of each cell in the overall architecture and enables parallel access to multiple cells' performance evaluation. During the J–V characterizations, dc biasing was applied to TE, and BE was kept grounded. All devices were dual swept from -1 to $+1$ V and back to -1 V at a fixed rate of 0.02 V s^{-1} under a current compliance (I_{CC}) of 1 mA to avoid permanent breakdown. For each ReRAM, first 20 consecutive voltage loops were recorded from the pristine state to confirm the absence of any high-voltage electroforming step [Fig. S3 in Supplementary Information]. The ReRAM device structures incorporating perovskite SL with varying PEABr and $EuBr_3$ molar stoichiometry that is, 1:1, 2:1, 3:1, and 4:1 2-D perovskite formulations exhibited forming-free operation, indicating that the intrinsic material properties provided sufficient pathways for ionic and electronic transport without the need for a high-voltage electroforming step and respectively, are denoted as D1, D2, D3, and D4 in the subsequent sections of this work.

The ReRAM D1 did not exhibit functional RS, with an LRS/HRS ratio of only ~1.26 [Fig. 3(c)], indicating negligible hysteresis. This behavior is consistent with the poor coverage and high roughness (Rq ~ 9.28 nm) observed in FESEM/AFM, and the presence of residual $EuBr_3$ phases in XRD. Large voids and exposed FTO regions act as direct low-resistance pathways between the electrodes, bypassing the semiconducting perovskite layer and enabling uncontrolled current percolation even under low bias. Increasing the ratio to 2:1 (D2) resulted in RS with a low SET voltage (V_S = 0.36 V) and an LRS/HRS ratio of 41.16; however, the RESET process was incomplete and significant leakage persisted in the nominal HRS, as shown in Fig. 3(d). The partial improvement in surface coverage (Rq ~ 3.51 nm) and moderate work function (ϕ_{Sample} ~ 4.43 eV) were insufficient to suppress nonuniform conduction through pinholes and grain-boundary discontinuities, as confirmed by the morphological analysis. Fig. 3(e) demonstrates that the 3:1 composition (D3) yielded the most stable and symmetric bipolar RS switching characteristics, with V_S = 0.48 V, V_R = −0.48 V, and an LRS/HRS ratio of 3003.35. This superior performance is attributed to the dense, pinhole-free morphology (Rq ~ 2.20 nm), complete suppression of $EuBr_3$-related peaks in XRD, optimal crystallographic ordering, and well-aligned surface dipoles (CPD ~ −308 mV; ϕ_{Sample} ~ 4.61 eV), which collectively ensure uniform electric field distribution and enable reproducible formation and disruption of conductive pathways within the active layer during dc bias loop. Further increasing the ratio to 4:1 (D4) maintained bipolar RS but required higher switching voltages (V_S = 0.88 V, V_R = −0.92 V) and yielded a reduced LRS/HRS ratio of 122.73 [Fig. 3(f)]. Although the work function reached its highest value (ϕ_{Sample} ~ 4.74 eV) due to denser surface dipoles, morphological degradation manifested as the form of multilayer island growth (Rq ~ 5.29 nm) may introduce localized electric field hot spots, increasing the voltage required for complete switching and reducing the resistance contrast.

Fig. 3(g) showed the retention behavior of Ag/PEABr:$EuBr_3$/FTO ReRAM devices (D1–D4), assessed over the monitored time window (26 000 s) at a read voltage of 0.1 V to evaluate the stability of both LRS and HRS, where the memory window is defined as $W = J_{LRS}/J_{HRS}$ (current densities in A·cm^{-2}). For quantitative comparison, the current density variation rate was expressed as $\%/_{decade}$ calculated from the slope of the $J - \log_{10}(t)$ fit normalized to the initial current density, following methods analogous to "decade-hour" [21]:

$$\%/_{decade} = \frac{\text{slope}\ \left(\text{A cm}^{-2}/\text{decade}\right)}{J_{initial}\ \left(\text{A cm}^{-2}\right)} \times 100. \quad (3)$$

Device D1 showed strong current instability in both resistance states, with J_{LRS} and J_{HRS} rising by +62.47% $decade^{-1}$ and +60.90% $decade^{-1}$, respectively. As a result, the two states merged across the entire retention window. Such simultaneous upward drift indicates that the device supports poorly regulated conduction paths, consistent with the surface discontinuities discussed earlier, which promote increasing leakage over time. For D2, the initial memory window was ~41.16, but the retention characteristics were highly unbalanced: J_{LRS} decreased at −53.83% $decade^{-1}$, whereas J_{HRS} continued to rise at +48.86% $decade^{-1}$, shrinking the window to ~2.08 by 26 000 s. Among all devices, D3 displayed the most stable behavior. J_{LRS} declined only slightly (−31.04% $decade^{-1}$) and J_{HRS} stayed nearly unchanged (+1.52% $decade^{-1}$). This stability is attributed to its smooth, defect-suppressed surface and well-aligned work function, which promotes a more uniform electric field and reduce unwanted carrier injection, thereby maintaining a well-defined OFF state. As shown in Fig. 3(g), D3 retained >90% of its LRS current for ~ 12 608 s before gradual decay, starting from an initial W ~ 3.0×10^3 and ending at W ~ 883.89 (a ~ 3.39× reduction). D4 exhibited moderate retention, with J_{LRS} decaying at −47.17% $decade^{-1}$ and J_{HRS} remaining nearly constant (−0.53% $decade^{-1}$). While it maintained stable retention for ~ 15 300 s before degradation onset, morphological disorder induced by excess PEABr likely deaccelerated LRS relaxation thereafter, leading to eventual J_{LRS}/J_{HRS} overlap near 26 000 s. These results indicate that while D3 provides the best long-term retention stability relative to its initial performance, D4 offers a significantly longer absolute stability period before J_{LRS} degraded to reach J_{HRS}, and D1 exhibited continuous overlapping in J_{LRS} and J_{HRS}.

The % $decade^{-1}$ value represents how quickly the LRS or HRS drifts per logarithmic decade of time, while the σ/μ% obtained from the cdf [Fig. 3(h) and (i)] indicates the spread around the mean, that is, the switching uniformity. Together, these metrics provide a complete picture of both the time-dependent drift (degradation) and the consistency of switching (variability). The σ/μ% values over ~26 000 s were for LRS: 20.72% (D1), 40.61% (D2), 27.69% (D3), and 44.93% (D4) [Fig. 3(h)]; and HRS: 21.10% (D1), 23.97% (D2), 14.44%

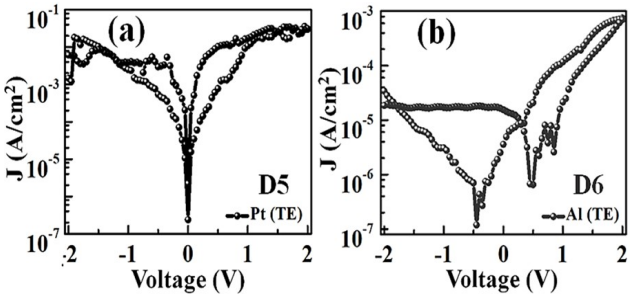

Fig. 4. Dual sweep J–V characteristics of (a) Pt/$(PEA)_3EuBr_6$/FTO, and (b) Al/$(PEA)_3EuBr_6$/FTO.

(D3), and 4.13% (D4) [Fig. 3(i)]. The low variability and moderate degradation rates in D3 validate its superior retention stability compared to the other devices, attributable to the $(PEA)_3EuBr_6$ 2-D perovskite SL derived from the optimized 3:1 PEABr:$EuBr_3$.

The endurance characteristics of the four ReRAM configurations were examined up to 40 000 cycles [Fig. 3(j)]. ReRAM D1 showed marked instability: the LRS current gradually declined (−15.72% decade^{-1}), whereas the HRS increased substantially (+88.10% decade^{-1}), causing the memory window to shrink until the two states eventually overlapped. D2 performed even worse, with both resistance states drifting upward during cycling (LRS: +86.78% decade^{-1}, HRS: +64.79% decade^{-1}), indicating uncontrolled leakage and explaining its weak retention behavior. In contrast, D3 demonstrated the most reliable endurance, preserving a wide window throughout repeated operation. Here, the LRS decreased moderately (−35.00% decade^{-1}) and the HRS also trended downward (−29.29% decade^{-1}), suggesting a comparatively stable filamentary process with limited parasitic leakage. D4 delivered intermediate stability, characterized by a stronger decay of the LRS (−62.44% decade^{-1}) and a slight reduction in the HRS (−7.99% decade^{-1}).

The σ/μ% for endurance cycles obtained from the cdf shown in Fig. 3(k) and (l). The σ/μ% values over ~40, 000 cycles were: for LRS: 11.07% (D1), 35.23% (D2), 26.39% (D3), and 61.55% (D4) [Fig. 3(k)]; and HRS: 21.07% (D1), 40.26% (D2), 26.34% (D3), and 15.92% (D4) [Fig. 3(l)]. The low variability and moderate degradation rates in D3 validate its superior endurance stability.

To clarify CF dynamics in the/PEA_3EuBr_6/FTO device (D3), two control devices with the same SL but different TEs were fabricated and characterized: Pt/$(PEA)_3EuBr_6$/FTO (D5) and Al/$(PEA)_3EuBr_6$/FTO (D6), with a common FTO BE. As shown in Fig. 4(a), D5 exhibits gradual, analog-like current modulation without distinct SET/RESET, unlike the abrupt bipolar switching in D3. This might stem from the large Schottky barrier at the Pt-perovskite interface (ϕ_Pt ~6.35 eV versus ϕ_SL ~4.61 eV), which suppresses carrier injection, lowers current density, and necessitates higher fields for conduction [22], [23]. Without active metal ions (Ag^+), resistance changes arise from defect-assisted transport through intrinsic traps [24].

In Fig. 4(b), D6 (Al/$(PEA)_3EuBr_6$/FTO) exhibits asymmetric switching and nonlinear conduction arising from the formation of a thin interfacial AlO_X layer during or after

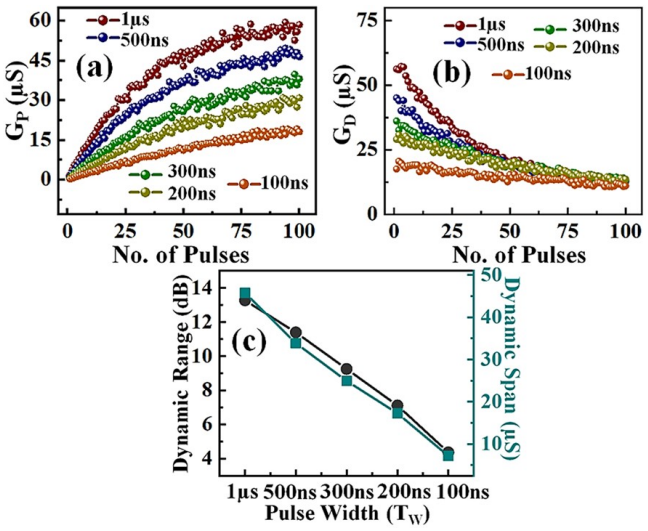

Fig. 5. (a) Synaptic potentiation, and (b) depression characteristics of the/PEA_3EuBr_6/FTO ReRAM (D3) under 100 identical ±0.5 V pulses at pulse widths from 1 μs to 100 ns. (c) DR (ΔG, DR) decreases systematically with pulse shortening, reflecting reduced modulation amplitude per programming event.

Al deposition. Because aluminum has a very high oxygen affinity (ΔG_f° [Al_2O_3] ≈ −1582 kJ mol^{-1}) [25], residual surface oxygen, adsorbed H_2O/OH^- groups, or halide species on the perovskite film readily react with incoming Al atoms, forming a self-limited Al_2O_3 barrier of ~1–3 nm [26]. This interfacial oxide behaves as an electronic tunneling barrier that impedes both carrier injection and Ag^+/halide migration, thereby suppressing CF growth and producing higher V_S together with rectifying J–V characteristics. Similar native AlO_X formation has been directly confirmed by XPS and TEM-EELS analyses at Al/perovskite and Al/oxide interfaces in related systems [26], [27], [28], corroborating this interpretation. These observations further confirm that robust bipolar RS in D3 originates from Ag-driven electrochemical metallization (ECM) processes, where reversible Ag^+ migration and reduction govern filament formation and rupture, whereas devices employing inert (Pt) or oxidizable (Al) electrodes exhibit slower, defect-limited conduction lacking discrete SET/RESET transitions.

Further, to confirm the sub-0.5 V switching in D3 ReRAM, we have included quantitative cycle-to-cycle and device-to-device reproducibility analyses. A representative D3 device was tested for 20 consecutive dual sweeps (−0.5 → +0.5 → −0.5 V, I_{CC} = 1 mA), yielding V_S = 0.42 ± 0.06 V and V_R = −0.44 ± 0.04 V. Additionally, 10 independent D3 cells exhibited V_S = 0.40 ± 0.08 V and V_R = −0.42 ± 0.06 V, all confined within ±0.5 V. These results confirm that the low-voltage switching is statistically reproducible across both cycles and devices. The corresponding plots have been added as Supplementary Information Fig. S4(a) and (b).

In potentiation mode [Fig. 5(a)], conductance increased monotonically with longer pulses, producing steeper slopes due to enhanced Ag^+ migration and more complete CF reinforcement per stimulus. The 1 μs pulsewidth increased conductance from ~1.79 to ~58.45 μS, corresponding to an average rate of +0.57 μS/pulse, whereas 100 ns pulses increased from ~0.31 to ~18.14 μS with a slower rate

of +0.12 μS/pulse, indicating a $\sim$ 4.75$\times$ reduction in modulation speed. During depression [Fig. 5(b)], the device conductance gradually decreased as additional pulses were applied, and the rate of decrease depended on the pulsewidth. Longer pulses produced a steeper drop in conductance (e.g., about -0.44 μS/pulse at 1 μs compared to -0.067 μS/pulse at 100 ns), indicating that wider pulses promote more pronounced filament dissolution in each step. In contrast, shorter pulses (<300 ns) resulted in smaller, more controlled conductance changes, enabling smoother and more symmetric weight adjustment.

Fig. 5(c) shows the variation in DR (ΔG in μS and DR in dB), which represents the ratio between the highest and lowest attainable conductance states. This parameter determines how effectively a synaptic device can encode a broad span of weights. A larger DR provides clearer separation between potentiated and depressed states, limiting overlap and generally improving neural-network inference accuracy. For the present device, the maximum DR is obtained under 1 μs programming pulses (45.77 μS; 13.27 dB). The values progressively decrease as the pulsewidth is shortened: 500 ns (33.86 μS; 11.39 dB), 300 ns (24.93 μS; 9.25 dB), 200 ns (17.24 μS; 7.11 dB), and 100 ns (7.16 μS; 4.36 dB). This behavior is directly linked to the reduced conductance increment per pulse at shorter durations, which limit the achievable modulation depth. Consequently, long pulses are more effective when wide weight separation is required, whereas short pulses provide finer control over incremental updates, which are advantageous for tasks that rely on precise analog tuning rather than large conductance swings.

Fig. 6(a)–(e) shows the NLI, evaluated only for potentiation. the NLI for potentiation decreases monotonically as the pulsewidth is reduced from 1 μs to 100 ns, indicating that shorter pulses facilitate a more linear conductance evolution, a critical property for achieving high-accuracy neuromorphic learning. In artificial synapses, linear and symmetric weight updates are essential to minimize training error and maintain convergence in learning algorithms. The NLI serves as a quantitative metric of this linearity, where lower values indicate that conductance changes follow the ideal linear trajectory more closely, thereby enabling more precise synaptic weight tuning in spiking neural networks (SNNs) and backpropagation-based systems [29].

In ECM-based ReRAM devices, potentiation occurs through the drift of Ag^+ ions and their subsequent reduction into metallic filaments. When relatively long voltage pulses (e.g., 1 μs) are applied, each pulse delivers more charge, which drives the filament to thicken rapidly at the beginning of potentiation. This leads to a fast rise in conductance followed by early saturation, producing a noticeable deviation from the ideal linear behavior and a corresponding increase in NLI. Shorter pulses (100–300 ns), however, limit the amount of charge available in each event. As a result, the filament extends in smaller increments, overshoot is suppressed, and the conductance evolves more gradually. This stepwise growth keeps the potentiation trace close to the ideal linear trend, with the best linearity (NLI = 0.14%) obtained at a 100 ns pulsewidth.

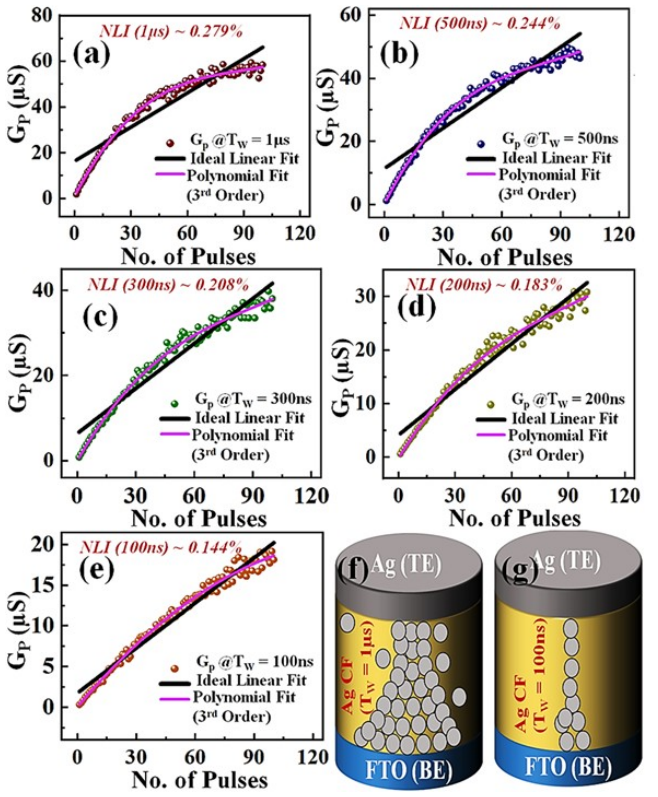

Fig. 6. (a)–(e) Potentiation nonlinearity (NLI) of the Ag/$(PEA)_3EuBr_6$/FTO device (D3) under different programming pulse widths, showing the dependence of conductance update behavior on pulse duration. (f) and (g) Schematic illustration of Ag-filament evolution in an ECM memristor: longer pulses allow the filament to thicken rapidly, while shorter pulses produce gradual, controlled filament growth.

This dependence on pulse duration is consistent with established ECM filament kinetics [30], where the morphology and growth rate of Ag filaments strongly depend on the temporal width of the applied stimulus. Long pulses favor rapid filament thickening and early saturation, whereas short pulses constrain the instantaneous ionic flux and promote controlled, layer-by-layer extension. The gradual improvement in linearity from an NLI of 0.00279 at 1 μs to 0.00144 at 100 ns, directly reflects the shift from rapid bulk growth to finely modulated filament evolution, as schematically illustrated in Fig. 6(f) and (g).

These results show that the timing of the programming pulses must be carefully controlled to obtain linear and balanced potentiation in ECM-based memristors, which is essential for reliable synaptic weight modulation in neuromorphic hardware.

III. Conclusion

In summary, this study demonstrates that careful precise stoichiometry control of the PEABr:$EuBr_3$ ratio plays a central role in defining the electrical behavior of Eu-based 2-D perovskite ReRAM. The 3:1 composition, in particular, yields films with improved surface quality, stronger crystallographic orientation, and favorable interfacial energetics, enabling forming-free operation, consistent sub-0.5 V switching, and a robust memory window of approximately 3.0×10^3. Electrode-dependent measurements further verify

an ECM-type switching process, where Ag^+ transport and subsequent reduction govern the formation and dissolution of conductive paths inside the $(PEA)_3EuBr_6$ lattice. Neuromorphic testing shows that longer write pulses broaden the DR but compromise linearity, whereas short pulses in the 100–300 ns range limit excessive filament growth and provide nearly linear synaptic weight updates with very low nonlinearity. This highlights that temporal pulse engineering offers a decisive means to balance DR and linearity trade-offs, enabling targeted optimization of device behavior for specific neuromorphic computing tasks. Thus, the optimized 3:1 $(PEA)_3EuBr_6$ SL in Ag-based ReRAM delivers sub-0.5 V symmetric ECM switching with exceptional retention ($>10^4$ s)/endurance ($>10^4$ cycles), while pulsewidth engineering enables tunable DR, linearity trade-offs, positioning this lead-free 2-D perovskite as a highly competent switching medium for both NV memory and neuromorphic computing applications.

Acknowledgment

The authors acknowledge the Centre for Design and Fabrication of Electronic Devices (C4DFED) and the Class 100 cleanroom facility at IIT Mandi, Mandi, India, for their support in sample preparation and electrical characterization. They also acknowledge the state-of-the-art FESEM facility available in C4DFED for nano-scale imaging and the chemical characterization facilities at the Advanced Material Research Centre (AMRC), IIT Mandi.

References

[1] J. J. Yang, "Special issue on neuromorphic computing, IEEE electron devices magazine [from the editor]," *IEEE Electron Devices Mag.*, vol. 1, no. 2, pp. 4–5, Sep. 2023, doi: 10.1109/MED.2023.3307978.

[2] M. Chauhan, S. Choudhary, and S. K. Sharma, "Reliable memristive switching empowered by Ag/NiO/W ReRAM configuration for multilevel non-volatile memory applications," *Adv. Electron. Mater.*, vol. 10, no. 4, Apr. 2024, Art. no. 2300724, doi: 10.1002/aelm.202300724.

[3] D. Ielmini, "Brain-inspired computing with resistive switching memory (RRAM): Devices, synapses and neural networks," *Microelectron. Eng.*, vol. 190, pp. 44–53, Apr. 2018, doi: 10.1016/j.mee.2018.01.009.

[4] M. Chauhan, R. Singh, and S. K. Sharma, "Electro-optically tunable passivated double-cation perovskite-based ReRAM for low-power memory applications," *ACS Appl. Electron. Mater.*, vol. 6, no. 4, pp. 2709–2719, Apr. 2024, doi: 10.1021/acsaelm.4c00257.

[5] R. Singh, M. Kundar, S. K. Pal, and S. K. Sharma, "Bandgap engineered double-cation/double-halide quasi-cubic perovskite for highly efficient (>36%) indoor photovoltaics," *IEEE J. Photovolt.*, vol. 13, no. 6, pp. 858–865, Nov. 2023, doi: 10.1109/JPHOTOV.2023.3300366.

[6] M. Kundar et al., "Surface passivation by sulfur-based 2D $(TEA)_2PbI_4$ for stable and efficient perovskite solar cells," *ACS Omega*, vol. 8, no. 14, pp. 12842–12852, Apr. 2023, doi: 10.1021/acsomega.2c08126.

[7] J. Di et al., "Two-dimensional $(C_6H_5C_2H_4NH_3)_2PbI_4$ perovskite single crystal resistive switching memory devices," *IEEE Electron Device Lett.*, vol. 42, no. 3, pp. 327–330, Mar. 2021, doi: 10.1109/LED.2021.3053009.

[8] X.-F. Cheng et al., "Pseudohalide-induced 2D $(CH_3NH_3)_2PbI_2(SCN)_2$ perovskite for ternary resistive memory with high performance," *Small*, vol. 14, no. 12, Mar. 2018, Art. no. 1703667.

[9] G. S. H. Thien et al., "Recent advances in halide perovskite resistive switching memory devices: A transformation from lead-based to lead-free perovskites," *ACS Omega*, vol. 7, no. 44, pp. 39472–39481, Nov. 2022, doi: 10.1021/acsomega.2c03206.

[10] P. J. Dereń, D. Stefańska, M. Ptak, and P. Wiśniewski, "Method to measure the degree of reduction of Eu^{3+} to Eu^{2+}: How anion and cation vacancies influence the degree of reduction," *J. Phys. Chem. C*, vol. 125, no. 44, pp. 24505–24514, Nov. 2021, doi: 10.1021/acs.jpcc.1c06977.

[11] M. Kirberger and J. J. Yang, "Structural differences between Pb^{2+}- and Ca^{2+}-binding sites in proteins: Implications with respect to toxicity," *J. Inorganic Biochem.*, vol. 102, no. 10, pp. 1901–1909, Oct. 2008, doi: 10.1016/j.jinorgbio.2008.06.014.

[12] M. Pazoki, A. Röckert, M. J. Wolf, R. Imani, T. Edvinsson, and J. Kullgren, "Electronic structure of organic–inorganic lanthanide iodide perovskite solar cell materials," *J. Mater. Chem. A*, vol. 5, no. 44, pp. 23131–23138, 2017, doi: 10.1039/c7ta07716e.

[13] M. Ban et al., "Solution-processed perovskite light emitting diodes with efficiency exceeding 15% through additive-controlled nanostructure tailoring," *Nature Commun.*, vol. 9, no. 1, p. 3892, Sep. 2018, doi: 10.1038/s41467-018-06425-5.

[14] Y. Zhang et al., "Two-dimensional $(PEA)_2PbBr_4$ perovskite single crystals for a high performance UV-detector," *J. Mater. Chem. C*, vol. 7, no. 6, pp. 1584–1591, 2019, doi: 10.1039/c8tc06129g.

[15] C. C. Stoumpos et al., "Ruddlesden–popper hybrid lead iodide perovskite 2D homologous semiconductors," *Chem. Mater.*, vol. 28, no. 8, pp. 2852–2867, Apr. 2016, doi: 10.1021/acs.chemmater.6b00847.

[16] R. Shendrik et al., "Optical and structural properties of Eu^{2+} doped BaBrI and BaClI crystals," *J. Lumin.*, vol. 192, pp. 653–660, Dec. 2017, doi: 10.1016/j.jlumin.2017.07.059.

[17] X. L. Quinn et al., "Europium addition reduces local structural disorder and enhances photoluminescent yield in perovskite $CsPbBr_3$," *Adv. Opt. Mater.*, vol. 9, no. 18, Sep. 2021, Art. no. 2002221, doi: 10.1002/adom.202002221.

[18] X. Gao et al., "Ruddlesden–popper perovskites: Synthesis and optical properties for optoelectronic applications," *Adv. Sci.*, vol. 6, no. 22, Nov. 2019, Art. no. 1900941, doi: 10.1002/advs.201900941.

[19] L. Canil et al., "Tuning halide perovskite energy levels," *Energy Environ. Sci.*, vol. 14, no. 3, pp. 1429–1438, Mar. 2021, doi: 10.1039/d0ee02216k.

[20] G. Çankaya and N. Uçar, "Schottky barrier height dependence on the metal work function for p-type Si Schottky diodes," *Zeitschrift für Naturforschung A*, vol. 59, no. 11, pp. 795–798, Nov. 2004. [Online]. Available: http://znaturforsch.com

[21] J. Prymak, M. Randall, P. Blais, and B. Long, "Why that 47 uF capacitor drops to 37 uF, 30 uF, or lower," in *Proc. 28th Symp. Passive Electron.*, 2008, pp. 1–14. [Online]. Available: https://www.researchgate.net/publication/229019152

[22] L. Chen, X. Li, G. Li, and W. Hu, "Contact property depending on radiation intensity between the perovskite semiconductor layer and electrode film," *Appl. Phys. Lett.*, vol. 121, no. 12, Sep. 2022, Art. no. 121601, doi: 10.1063/5.0114047.

[23] E. Paz Totolhua et al., "Enhanced efficiency of mixed-halide perovskite solar cells through optimization of the layer thicknesses, defect density, and metal contact work function," *Materials*, vol. 18, no. 7, p. 1601, Apr. 2025, doi: 10.3390/ma18071601.

[24] R. Waser, R. Dittmann, G. Staikov, and K. Szot, "Redox-based resistive switching memories—Nanoionic mechanisms, prospects, and challenges," *Adv. Mater.*, vol. 21, nos. 25–26, pp. 2632–2663, Jul. 2009, doi: 10.1002/adma.200900375.

[25] E. Ziyekile. *Thermodynamic Data at 25°C for Inorganic & Organic Substances*. Cape Peninsula University of Technology. Accessed: Nov. 13, 2025. [Online]. Available: https://www.studocu.com/en-za/document/cape-peninsula-university-of-technology/thermodynamics/thermodynamic-data-at-250c-for-inorganic-organic-substances/137976139

[26] B. Nath, P. C. Ramamurthy, G. Hegde, and D. Roy Mahapatra, "Role of electrodes on perovskite solar cells performance: A review," *ISSS J. Micro Smart Syst.*, vol. 11, no. 1, pp. 61–79, Jun. 2022, doi: 10.1007/s41683-021-00089-y.

[27] D. Koushik et al., "Chemical analysis of the interface between hybrid organic–inorganic perovskite and atomic layer deposited Al_2O_3," *ACS Appl. Mater. Interfaces*, vol. 11, no. 5, pp. 5526–5535, Feb. 2019, doi: 10.1021/acsami.8b18307.

[28] R. Zhao et al., "Surface passivation of organometal halide perovskites by atomic layer deposition: An investigation of the mechanism of efficient inverted planar solar cells," *Nanosc. Adv.*, vol. 3, no. 8, pp. 2305–2315, Apr. 2021, doi: 10.1039/d1na00075f.

[29] S. Brivio, D. R. B. Ly, E. Vianello, and S. Spiga, "Non-linear memristive synaptic dynamics for efficient unsupervised learning in spiking neural networks," *Frontiers Neurosci.*, vol. 15, Feb. 2021, Art. no. 580909, doi: 10.3389/fnins.2021.580909.

[30] S. Menzel, S. Tappertzhofen, R. Waser, and I. Valov, "Switching kinetics of electrochemical metallization memory cells," *Phys. Chem. Chem. Phys.*, vol. 15, no. 18, pp. 6945–6952, Apr. 2013, doi: 10.1039/c3cp50738f.